Mode-Selective Elastic Metasurfaces

Sung Won Lee[ ],[1] Seung Il Kim,[2,3] Hong Min Seung[ ],[2,3] and Joo Hwan Oh[ ][1,*]

[1]*School of Mechanical Engineering, Ulsan National Institute of Science and Technology, UNIST-gil 50, Eonyang-eup, Ulju-gun, Ulsan 44919, South Korea*

[2]*Intelligent Wave Engineering Team, Korea Research Institute of Standards and Science, Daejeon, 34113, Republic of Korea*

[3]*Department of Precision Measurement, University of Science and Technology (UST), Daejeon, 34113, Republic of Korea*

The existence of multimodes is a unique characteristic of various elastic wave systems, including elastic metasurfaces. Nevertheless, most of the previous research on elastic metasurfaces has focused on a single mode only, so the related physics is largely unknown and noise is generated by the undesired incident wave mode. Here, we present a mode-selective elastic metasurface that can tailor the target wave mode while filtering out the undesired wave mode. To this end, analytical investigation is carried out for an elastic metasurface with multimode incidence such that the metasurface can operate for both longitudinal and shear wave modes. After that, the mode-selective elastic metasurface is designed and validated numerically and experimentally. With our research, it is now possible to explicitly design an elastic metasurface for the multimode incidence case. Furthermore, since the noise caused by the undesired wave mode is barely generated with the proposed mode-selective metasurface, various elastic wave devices and physical findings are expected from the current research.

I. INTRODUCTION

Metasurfaces [1–4] are artificial subwavelength layers designed with the purpose of tailoring a wavefront. Recently, metasurfaces have attracted much attention in various areas of wave physics owing to their capability of realizing convenient and extraordinary wave phenomena at boundaries or interfaces, such as anomalous reflection and refraction [5–10], impedance matching [11–14], holography [15–18], or cloaking [19–22] within very compact devices. In particular, elastic metasurfaces have been independently studied in the fields of acoustic or electromagnetic metasurfaces owing to their unique tensorial physics. Naming a few, Lee *et al*. [23] and Lee [24] successfully realized wave tailoring of longitudinal waves with full transmission by subwavelength arrays or single resonator structures. Su *et al.* [25] and Zhang *et al.* [26] tailored shear waves using simple flexural slits. Cao *et al.* designed a pillared elastic metasurface [27] to deflect flexural waves and enhanced its performance using constructive interference [28].

However, although what makes elastic metasurfaces different from acoustic or electromagnetic metasurfaces is the characteristic of multimodes, previous works have usually focused on the single incident wave mode case only.

For instance, Kim *et al*. [29] and Lee *et al*. [30] realized perfect mode conversion from longitudinal wave to shear wave using the generalized Snell's law concept and mode coupling between the two waves. Cao *et al*. [31] successfully realized perfect mode conversion between longitudinal wave and flexural wave, which was called a trapped mode with perfect mode conversion. However, single wave mode incidence has been considered in these studies so that if another wave mode is incident, the metasurface does not work and the wave is randomly scattered. Recently, Rong and Ye [32] used topology optimization to achieve an elastic metasurface for both longitudinal and shear incident wave cases. Unfortunately, owing to the limitation of the topology optimization, the background physics and detailed design guidelines are insufficiently provided, which demands to achieve elastic metasurfaces considering the multimode incidence case with clear operating physics. In particular, if an elastic metasurface that can tailor the desired wave mode and filter out the undesired wave mode becomes possible, the aforementioned scattering issue can be solved.

Here, in this work, a mode-selective metasurface that can tailor the desired wave mode but filter out the undesired wave mode is proposed. To this end, we develop a theory of elastic metasurfaces operating for both longitudinal and shear wave incidence cases so that any metasurface can be explicitly designed for multimode

_____

*joohwan.oh@unist.ac.kr

incident cases. Our theory and metasurface are based on a single-unit elastic metasurface [24], i.e., we suggest a single-unit metasurface that can tailor both longitudinal and shear waves with the desired transmission and phase shift and we provide a theoretical explanation. While the previous research [24] has considered longitudinal wave incidence only, we find that a single-unit metasurface is also possible for the shear wave incidence case by utilizing rotational and vertical resonances. Accordingly, any desired phase shifts are achievable with a single unit for not only longitudinal but also shear wave incidence cases. With the findings, we establish a theory and design guidelines for a single-unit metasurface for both longitudinal and shear waves.

Based on the theory, we design mode-selective metasurfaces using the single-unit elastic metasurface for multimode incidence cases. To design the mode-selective metasurface, each unit is designed to provide the desired phase shift and 100% transmission for the desired wave mode, but 0% transmission for the undesired wave mode. With numerical and experimental support, the performance of the mode-selective metasurface is validated. The validations clearly support that our approach to the multimode elastic metasurface can be effectively applied to various cases where multiple wave modes are involved.

This paper is organized as follows. First, we analyze the theoretical condition of full transmission with desired phase shift for both longitudinal and shear waves. To realize the demanded effective parameters, we design a single mass-spring resonator, which is capable of tuning both longitudinal and shear effective parameters, and demonstrate the mechanism. Finally, we design two types of mode-selective metasurface that steer the desired mode under full transmission, fully reflecting the other mode. The two designed metasurfaces are validated by numerical wave field simulations and experiments.

II. THEORETICAL BACKGROUND

A. Effective parameter conditions for various phase shifts under full transmission

To achieve an elastic metasurface under the multimode incidence condition, the metasurfaces' unit cell should be designed to achieve the desired phase shift and transmission for both longitudinal and shear wave modes simultaneously. In this section, we explain how these conditions can be satisfied for both wave modes with a mass-spring system. Figure 1 shows a schematic diagram of a single mass-spring system for both longitudinal and shear waves, where u, v, f_x, and f_y refer to the horizontal and vertical displacements and forces, respectively, while the subscripts o and d indicate that the variable is defined at the left or right side of the mass-spring system. Additionally, α_{eff} and β_{eff} refer to the longitudinal and shear effective stiffness, while m_L and m_S refer to the longitudinal and shear effective
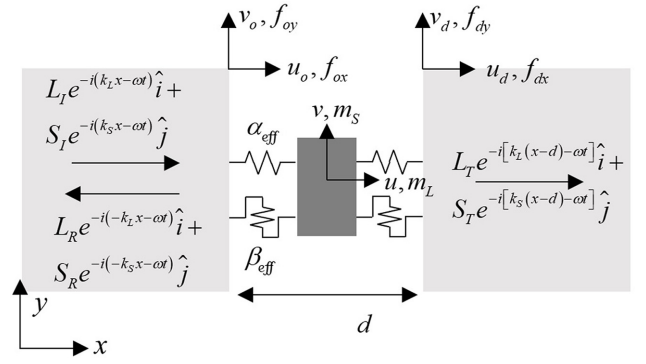

FIG. 1. The schematic figure of a single mass-spring system for multimode incident case.

mass. The x- and y-directional equations of the mass-spring unit can be derived as

$$m_L \ddot{u} = \alpha_{\text{eff}}(u_o - 2u + u_d), \tag{1a}$$

$$m_S \ddot{v} = \beta_{\text{eff}}(v_o - 2v + v_d), \tag{1b}$$

$$f_{ox} = \alpha_{\text{eff}}(u - u_o), \tag{2a}$$

$$f_{dx} = \alpha_{\text{eff}}(u_d - u), \tag{2b}$$

$$f_{oy} = \beta_{\text{eff}}(v - v_o), \tag{3a}$$

$$f_{dy} = \beta_{\text{eff}}(v_d - v). \tag{3b}$$

Assuming a simple harmonic motion with an angular frequency ω, Eqs. (1)–(3) can be rearranged into linear equations as

$$u = \frac{\alpha_{\text{eff}}}{2\alpha_{\text{eff}} - \omega^2 m_L}(u_o + u_d), \tag{4a}$$

$$v = \frac{\beta_{\text{eff}}}{2\beta_{\text{eff}} - \omega^2 m_S}(v_o + v_d), \tag{4b}$$

$$u_d = \frac{\alpha_{\text{eff}} - \omega^2 m_L}{\alpha_{\text{eff}}}u_o + \frac{2\alpha_{\text{eff}} - \omega^2 m_L}{\alpha_{\text{eff}}^2}f_{ox}, \tag{5a}$$

$$v_d = \frac{\beta_{\text{eff}} - \omega^2 m_S}{\beta_{\text{eff}}}v_o + \frac{2\beta_{\text{eff}} - \omega^2 m_S}{\beta_{\text{eff}}^2}f_{oy}, \tag{5b}$$

$$f_{dx} = -\omega^2 m_L u_o + \frac{\alpha_{\text{eff}} - \omega^2 m_L}{\alpha_{\text{eff}}}f_{ox}, \tag{6a}$$

$$f_{dy} = -\omega^2 m_S u_o + \frac{\beta_{\text{eff}} - \omega^2 m_S}{\beta_{\text{eff}}}f_{oy}. \tag{6b}$$

Therefore, the boundary conditions at the left and right sides can be described in a matrix form, which is well-known as the transfer matrix [23,24], as

$$\begin{pmatrix} u_d \\ f_{dx} \end{pmatrix} = \mathbf{T}_L \begin{pmatrix} u_o \\ f_{ox} \end{pmatrix}, \mathbf{T}_L = \begin{pmatrix} \frac{\alpha_{\text{eff}} - \omega^2 m_L}{\alpha_{\text{eff}}} & \frac{2\alpha_{\text{eff}} - \omega^2 m_L}{\alpha_{\text{eff}}^2} \\ -\omega^2 m_L & \frac{\alpha_{\text{eff}} - \omega^2 m_L}{\alpha_{\text{eff}}} \end{pmatrix}$$

$$= \begin{pmatrix} T_{L11} & T_{L12} \\ T_{L21} & T_{L22} \end{pmatrix}, \qquad (7)$$

$$\begin{pmatrix} v_d \\ f_{dy} \end{pmatrix} = \mathbf{T}_S \begin{pmatrix} v_o \\ f_{oy} \end{pmatrix}, \mathbf{T}_S = \begin{pmatrix} \frac{\beta_{\text{eff}} - \omega^2 m_S}{\beta_{\text{eff}}} & \frac{2\beta_{\text{eff}} - \omega^2 m_S}{\beta_{\text{eff}}^2} \\ -\omega^2 m_S & \frac{\beta_{\text{eff}} - \omega^2 m_S}{\beta_{\text{eff}}} \end{pmatrix}$$

$$= \begin{pmatrix} T_{S11} & T_{S12} \\ T_{S21} & T_{S22} \end{pmatrix}. \qquad (8)$$

Now, let us focus on the wave mediums at the left and right sides. The displacements at each side can be written as:

(a) At the left medium

$$u_i = L_I e^{-i(k_L x - \omega t)} + L_R e^{-i(-k_L x - \omega t)}, \qquad (9)$$

$$v_i = S_I e^{-i(k_S x - \omega t)} + S_R e^{-i(-k_S x - \omega t)} \qquad (10)$$

(b) At the right medium

$$u_t = L_T e^{-i[k_L(x-d) - \omega t]}, \qquad (11)$$

$$v_t = S_T e^{-i[k_S(x-d) - \omega t]} \qquad (12)$$

where L and S are the longitudinal and shear amplitudes shown in Fig. 1. The subscripts l and r refers to the left and right field deformation. The subscripts I, R, and T refer to the incident, reflected, and transmitted amplitudes, respectively, and k_L and k_S indicate the wave number for longitudinal and shear waves, respectively. From the displacement fields in Eqs. (9)–(12), the longitudinal and shear traction forces can be calculated by using the longitudinal and shear impedances of the wave medium. Setting the longitudinal and shear impedances as Z_L and Z_S, the displacements and the traction forces can be derived as follows:

(a) At the left medium

$$\begin{pmatrix} u_i \\ f_{ix} \end{pmatrix} = \begin{pmatrix} e^{-ik_L x} & e^{ik_L x} \\ -i\omega Z_L e^{-ik_L x} & i\omega Z_L e^{ik_L x} \end{pmatrix} \begin{pmatrix} L_I \\ L_T \end{pmatrix} e^{i\omega t}, \quad (13a)$$

$$\begin{pmatrix} v_i \\ f_{iy} \end{pmatrix} = \begin{pmatrix} e^{-ik_S x} & e^{ik_S x} \\ -i\omega Z_S e^{-ik_S x} & i\omega Z_S e^{ik_S x} \end{pmatrix} \begin{pmatrix} S_I \\ S_T \end{pmatrix} e^{i\omega t} \quad (13b)$$

(b) At the right medium

$$\begin{pmatrix} u_t \\ f_{tx} \end{pmatrix} = \begin{pmatrix} e^{-ik_L(x-d)} & e^{ik_L(x-d)} \\ -i\omega Z_L e^{-ik_L(x-d)} & i\omega Z_L e^{ik_L(x-d)} \end{pmatrix} \begin{pmatrix} L_T \\ 0 \end{pmatrix} e^{i\omega t},$$
$$(14a)$$

$$\begin{pmatrix} v_t \\ f_{ty} \end{pmatrix} = \begin{pmatrix} e^{-ik_S(x-d)} & e^{ik_S(x-d)} \\ -i\omega Z_S e^{-ik_S(x-d)} & i\omega Z_S e^{ik_S(x-d)} \end{pmatrix} \begin{pmatrix} S_T \\ 0 \end{pmatrix} e^{i\omega t}$$
$$(14b)$$

By substituting $x = 0$ and $x = d$, Eqs. (13) and (14) can be rearranged as

$$\begin{pmatrix} u_o \\ f_{ox} \end{pmatrix} = \mathbf{M}_L \begin{pmatrix} L_I \\ L_R \end{pmatrix} e^{i\omega t}, \qquad (15a)$$

$$\begin{pmatrix} u_d \\ f_{dx} \end{pmatrix} = \mathbf{M}_L \begin{pmatrix} L_T \\ 0 \end{pmatrix} e^{i\omega t}, \qquad (15b)$$

$$\begin{pmatrix} v_o \\ f_{oy} \end{pmatrix} = \mathbf{M}_S \begin{pmatrix} S_I \\ S_R \end{pmatrix} e^{i\omega t}, \qquad (16a)$$

$$\begin{pmatrix} v_d \\ f_{dy} \end{pmatrix} = \mathbf{M}_S \begin{pmatrix} S_T \\ 0 \end{pmatrix} e^{i\omega t}, \qquad (16b)$$

where

$$\mathbf{M}_L = \begin{pmatrix} 1 & 1 \\ -i\omega Z_L & i\omega Z_L \end{pmatrix} \text{ and } \mathbf{M}_S = \begin{pmatrix} 1 & 1 \\ -i\omega Z_S & i\omega Z_S \end{pmatrix}. \qquad (17)$$

By inputting Eqs. (15) and (16) into Eqs. (7) and (8), one can obtain the matrix relation between amplitudes as

$$\begin{pmatrix} L_T \\ 0 \end{pmatrix} = \mathbf{M}_L^{-1} \mathbf{T}_L \mathbf{M}_L \begin{pmatrix} L_I \\ L_R \end{pmatrix} = \mathbf{L} \begin{pmatrix} L_I \\ L_R \end{pmatrix}, \qquad (18a)$$

$$\begin{pmatrix} S_T \\ 0 \end{pmatrix} = \mathbf{M}_S^{-1} \mathbf{T}_S \mathbf{M}_S \begin{pmatrix} S_I \\ S_R \end{pmatrix} = \mathbf{S} \begin{pmatrix} S_I \\ S_R \end{pmatrix}, \qquad (18b)$$

where

$$L_{11} = \frac{i\omega Z_L(T_{L11} + T_{L22}) - T_{L21} + \omega^2 Z_L^2 T_{L12}}{2i\omega Z_L}, \quad (19a)$$

$$L_{12} = \frac{i\omega Z_L(T_{L11} - T_{L22}) - T_{L21} - \omega^2 Z_L^2 T_{L12}}{2i\omega Z_L}, \quad (19b)$$

$$L_{21} = \frac{i\omega Z_L(T_{L11} - T_{L22}) + T_{L21} + \omega^2 Z_L^2 T_{L12}}{2i\omega Z_L}, \quad (19c)$$

$$L_{22} = \frac{i\omega Z_L(T_{L11} + T_{L22}) + T_{L21} - \omega^2 Z_L^2 T_{L12}}{2i\omega Z_L}, \quad (19d)$$

and

$$S_{11} = \frac{i\omega Z_S(T_{S11} + T_{S22}) - T_{S21} + \omega^2 Z_S^2 T_{S12}}{2i\omega Z_S}, \quad (20a)$$

$$S_{12} = \frac{i\omega Z_S(T_{S11} - T_{S22}) - T_{S21} - \omega^2 Z_S^2 T_{S12}}{2i\omega Z_S}, \quad (20b)$$

$$S_{21} = \frac{i\omega Z_S(T_{S11} - T_{S22}) + T_{S21} + \omega^2 Z_S^2 T_{S12}}{2i\omega Z_S}, \quad (20c)$$

$$S_{22} = \frac{i\omega Z_S(T_{S11} + T_{S22}) + T_{S21} - \omega^2 Z_S^2 T_{S12}}{2i\omega Z_S}. \quad (20d)$$

Note that the determinants of **L** and **S** are 1. From the inverse matrices of **L** and **S**, Eqs. (18a) and (18b) can be rearranged as

$$\begin{pmatrix} L_I \\ L_R \end{pmatrix} = \begin{pmatrix} L_{22} & -L_{12} \\ -L_{21} & L_{11} \end{pmatrix} \begin{pmatrix} L_T \\ 0 \end{pmatrix}, \quad (21a)$$

$$\begin{pmatrix} S_I \\ S_R \end{pmatrix} = \begin{pmatrix} S_{22} & -S_{12} \\ -S_{21} & S_{11} \end{pmatrix} \begin{pmatrix} S_T \\ 0 \end{pmatrix}. \quad (21b)$$

With the equations in Eq. (21), transmission and phase shifts for each mode are studied. First, let us focus on the transmission coefficient of the longitudinal wave. From Eq. (21a), the transmission coefficient T_L is derived as

$$T_L = L_T/L_I = \frac{1}{L_{22}}$$
$$= \frac{2i\omega Z_L}{i\omega Z_L(T_{L11} + T_{L22}) + T_{L21} - \omega^2 Z_L^2 T_{L12}}. \quad (22)$$

Considering $T_{L11} = T_{L22}$, Eq. (22) can be simplified as

$$T_L = \frac{1}{T_{L11} + \frac{i}{2}\left(-\frac{T_{L21}}{\omega Z_L} + \omega Z_L T_{L12}\right)}. \quad (23)$$

To simplify Eq. (23), the square of T_L is considered to get rid of any imaginary value as

$$|T_L|^2 = \frac{1}{T_{L11}^2 + (1/4)(-(T_{L21}/\omega Z_L) + \omega Z_L T_{L12})^2}. \quad (24)$$

Considering the determinant of the transfer matrix is 1, i.e., $T_{L11}^2 = T_{L12}T_{L21} + 1$, Eq. (24) can be rearranged as

$$|T_L|^2 = \frac{1}{1 + (1/4)((T_{L21}/\omega Z_L) + \omega Z_L T_{L12})^2}. \quad (25)$$

In the metasurface tailoring refracted longitudinal waves, each unit should satisfy the full transmission condition, $T_L = 1$. Therefore, to realize the full transmission, $(T_{L21}/\omega Z_L) + \omega Z_L T_{12}$ should be zero. With Eq. (7), the full transmission condition can be estimated as

$$\frac{T_{L21}}{\omega Z_L} + \omega Z_L T_{L12} = -\frac{\omega m_L}{Z_L} + \omega Z_L\left(\frac{2\alpha_{\text{eff}} - \omega^2 m_L}{\alpha_{\text{eff}}^2}\right) = 0. \quad (26)$$

Therefore, the full transmission can be achieved if and only if

$$m_L = \frac{2Z_L^2 \alpha_{\text{eff}}}{\alpha_{\text{eff}}^2 + \omega^2 Z_L^2}. \quad (27)$$

With the full transmission condition, the phase shift can be calculated. Substituting the full transmission condition $(T_{L21}/\omega Z_L) + \omega Z_L T_{L12} = 0$, Eq. (23) is simplified as

$$T_L = \frac{1}{T_{L11} + (i/2)(-(T_{L21}/\omega Z_L) + \omega Z_L T_{L12})}$$
$$= \frac{T_{L11} - (i/2)(-(T_{L21}/\omega Z_L) + \omega Z_L T_{L12})}{1 + (1/4)((T_{L21}/\omega Z_L) + \omega Z_L T_{L12})^2}$$
$$= T_{L11} + i\frac{T_{L21}}{\omega Z_L}. \quad (28)$$

In addition, Eq. (28) can be further simplified by substituting Eqs. (7) and (27) as

$$T_L = \frac{\alpha_{\text{eff}}^2 - \omega^2 Z_L^2}{\alpha_{\text{eff}}^2 + \omega^2 Z_L^2} - \frac{2\alpha_{\text{eff}} Z_L \omega}{\alpha_{\text{eff}}^2 + \omega^2 Z_L^2}i. \quad (29)$$

Accordingly, the longitudinal transmitted phase shift can be calculated as

$$\phi_L = \arg\left(\frac{\alpha_{\text{eff}}^2 - \omega^2 Z_L^2}{\alpha_{\text{eff}}^2 + \omega^2 Z_L^2} - \frac{2\alpha_{\text{eff}} Z_L \omega}{\alpha_{\text{eff}}^2 + \omega^2 Z_L^2}i\right). \quad (30)$$

Now, let us focus on the transmission coefficient of the shear wave. Note that from Eq. (7), the equations for the shear wave are similar to the equation for the longitudinal wave. Thus, following similar procedures, the following equations can be derived for the full transmission condition

as

$$m_S = \frac{2Z_S{}^2\beta_{\text{eff}}}{\beta_{\text{eff}}{}^2 + \omega^2 Z_S{}^2}, \tag{31a}$$

$$\phi_S = \arg\left(\frac{\beta_{\text{eff}}{}^2 - \omega^2 Z_S{}^2}{\beta_{\text{eff}}{}^2 + \omega^2 Z_S{}^2} - \frac{2\beta_{\text{eff}}Z_S\omega}{\beta_{\text{eff}}{}^2 + \omega^2 Z_S{}^2}i\right). \tag{31b}$$

In conclusion, the effective mass and spring coefficients required to achieve both the full transmission and the desired phase shifts ϕ_L and ϕ_S are summarized as

$$\alpha_{\text{eff}} = -\cot\left(\frac{\phi_L}{2}\right)\omega Z_L, \tag{32a}$$

$$m_L = -\frac{\sin(\phi_L)Z_L}{\omega}, \tag{32b}$$

$$\beta_{\text{eff}} = -\cot\left(\frac{\phi_S}{2}\right)\omega Z_S, \tag{33a}$$

$$m_S = -\frac{\sin(\phi_S)Z_S}{\omega}. \tag{33b}$$

In metasurfaces, various units should be designed to cover various phase shifts from 0 to 2π, i.e., ϕ_L and ϕ_S should be varied from 0 to 2π. This indicates that the effective parameters should be adjusted from negative to positive values. As a result, we conclude that to achieve an elastic metasurface in the multimode case, a metasurface unit whose effective mass and stiffness (for both longitudinal and shear waves) can be adjusted from negative to positive values is essential.

B. Metasurface unit demonstration

As explained previously, what we need to achieve for an elastic metasurface for multimode incidence is a metasurface unit whose effective mass and stiffness for both wave modes can be adjusted from negative to positive values. To achieve such a metasurface unit, we adopt the previously studied resonator system [24,30]. However, whereas the previous studies tuned the metasurface for the longitudinal mode only, here we expand its application to the shear mode. Figure 2(a) shows the schematics of the resonator system composed of the vertical resonators with m_2 and the inner resonator with m_1. Note that, unlike the longitudinal mode, which is governed by longitudinal motions as in Fig. 2(b), the shear mode involves both the vertical motions and various rotational motions, including the rotational motion of each mass, pairs of masses, or the whole structure. Among these various resonance modes, we choose the resonance motion shown in Fig. 2(c), which is shown to be suitable for shear wave manipulation.

Here, to consider both longitudinal and shear waves, all springs are expressed with 2×2 matrix spring coefficients. Since we are considering both longitudinal and
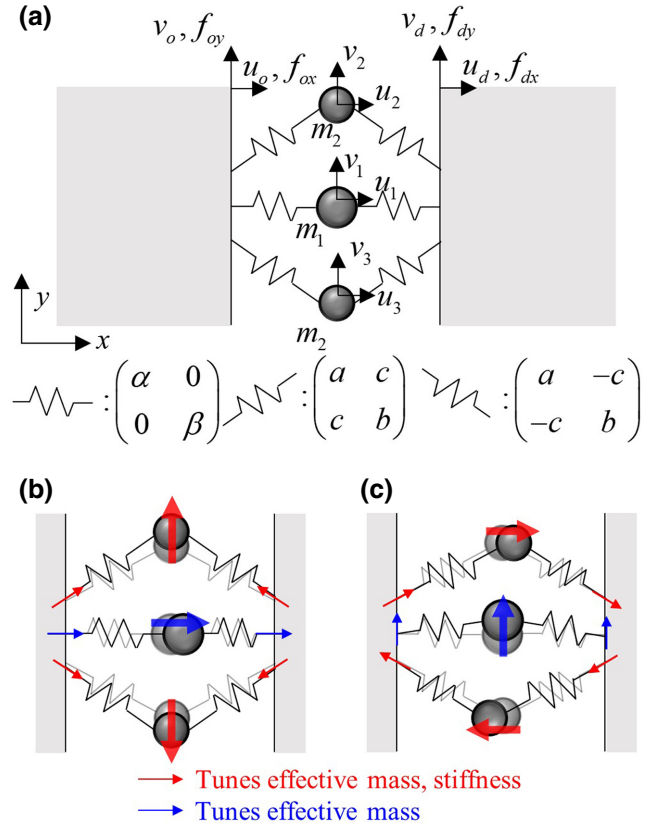

FIG. 2. (a) The schematic figure of the resonator system that can tune the longitudinal and shear effective parameters, and corresponding motions for (b) longitudinal and (c) shear resonances.

shear waves, both the horizontal and shear forces and displacements should be considered. Thus, each spring has longitudinal, shear, and coupled stiffness, which can be expressed in the 2×2 matrix form. For instance, the inner resonator horizontal beam can be explained as

$$\begin{pmatrix} F_x \\ F_y \end{pmatrix} = \begin{pmatrix} \alpha & 0 \\ 0 & \beta \end{pmatrix}\begin{pmatrix} u \\ v \end{pmatrix}, \tag{33}$$

since in the horizontal spring, the coupling between horizontal and vertical displacements is almost negligible. Similarly, the diagonal spring structures can be expressed in 2×2 spring matrix that have a nonzero off-diagonal term since the vertical and horizontal displacements and forces are coupled as

$$\begin{pmatrix} F_x \\ F_y \end{pmatrix} = \begin{pmatrix} a & c \\ c & b \end{pmatrix}\begin{pmatrix} u \\ v \end{pmatrix} \text{ or } \begin{pmatrix} F_x \\ F_y \end{pmatrix} = \begin{pmatrix} a & -c \\ -c & b \end{pmatrix}\begin{pmatrix} u \\ v \end{pmatrix}. \tag{34}$$

Assuming time-harmonic solutions, the equations of the motion for each resonator can be expressed as

$$-\omega^2 m_1 u_1 = \alpha(u_o - 2u_1 + u_d), \tag{35a}$$

$$-\omega^2 m_1 v_1 = \beta(v_o - 2v_1 + v_d), \tag{35b}$$

$$-\omega^2 m_2 u_2 = a(u_o - 2u_2 + u_d) + c(v_o - v_d), \tag{35c}$$

$$-\omega^2 m_2 v_2 = b(v_o - 2v_2 + v_d) + c(u_o - u_d), \tag{35d}$$

$$-\omega^2 m_2 u_3 = a(u_o - 2u_3 + u_d) + c(-v_o + v_d), \tag{35e}$$

$$-\omega^2 m_2 v_3 = b(v_o - 2v_3 + v_d) + c(-u_o + u_d). \tag{35f}$$

In addition, the forces at the left and right boundaries can be calculated as

$$f_{ox} = \alpha(-u_o + u_1) + a(-2u_o + u_2 + u_3) + c(v_2 - v_3), \tag{36a}$$

$$f_{dx} = \alpha(-u_1 + u_d) + a(-u_2 - u_3 + 2u_d) + c(v_2 - v_3), \tag{36b}$$

$$f_{oy} = \beta(-v_o + v_1) + b(-2v_o + v_2 + v_3) + c(u_2 - u_3), \tag{36c}$$

$$f_{dy} = \beta(-v_1 + v_d) + b(-v_2 - v_3 + 2v_d) + c(u_2 - u_3). \tag{36d}$$

By rearranging Eqs. (35a)–(35f), one can simplify the vertical and horizontal displacements of each mass as

$$u_1 = \frac{\alpha}{2\alpha - \omega^2 m_1}(u_o + u_d) = r_\alpha(u_o + u_d), \tag{37a}$$

$$v_1 = \frac{\beta}{2\beta - \omega^2 m_1}(v_o + v_d) = r_\beta(v_o + v_d), \tag{37b}$$

$$u_2 + u_3 = \frac{2a}{2a - \omega^2 m_2}(u_o + u_d) = r_a(u_o + u_d), \tag{37c}$$

$$u_2 - u_3 = \frac{2c}{2a - \omega^2 m_2}(v_o - v_d) = \frac{c}{a}r_a(v_o - v_d), \tag{37d}$$

$$v_2 + v_3 = \frac{2b}{2b - \omega^2 m_2}(v_o + v_d) = r_b(v_o + v_d), \tag{37e}$$

$$v_2 - v_3 = \frac{2c}{2b - \omega^2 m_2}(u_o - u_d) = \frac{c}{b}r_b(u_o - u_d). \tag{37f}$$

Note that for convenience, resonance terms are introduced as

$$r_\alpha = \frac{\alpha}{2\alpha - \omega^2 m_1}, \tag{38a}$$

$$r_\beta = \frac{\beta}{2\beta - \omega^2 m_1}, \tag{38b}$$

$$r_a = \frac{2a}{2a - \omega^2 m_2}, \tag{38c}$$

$$r_b = \frac{2b}{2b - \omega^2 m_2}. \tag{38d}$$

Substituting Eqs. (37a)–(37f) into Eqs. (36a)–(36d), the boundary traction forces can be expressed as a function of the displacements as

$$f_{ox} = \alpha(-u_o + r_\alpha u_o + r_\alpha u_d) + a(-2u_o + r_a(u_o + u_d))$$
$$+ \frac{c^2}{b}r_b(u_o - u_d), \tag{39a}$$

$$f_{dx} = \alpha(-r_\alpha u_o - r_\alpha u_d + u_d) + a(-r_a(u_o + u_d) + 2u_d)$$
$$+ \frac{c^2}{b}r_b(u_o - u_d), \tag{39b}$$

$$f_{oy} = \beta(-v_o + r_\beta v_o + r_\beta v_d) + b(-2v_o + r_b(v_o + v_d))$$
$$+ \frac{c^2}{a}r_a(v_o - v_d), \tag{39c}$$

$$f_{dy} = \beta(-r_\beta v_o - r_\beta v_d + v_d) + b(-r_b(v_o + v_d) + 2v_d)$$
$$+ \frac{c^2}{a}r_a(v_o - v_d). \tag{39d}$$

To figure out the relationship between the effective parameters and the mass-spring system, Eqs. (39a)–(39d) are rearranged in the form of the transfer matrix as

$$u_d = T_{L11}u_o + T_{L12}f_{ox}, \tag{40a}$$

$$f_{dx} = T_{L21}u_o + T_{L22}f_{ox}, \tag{40b}$$

$$v_d = T_{S11}v_o + T_{S12}f_{oy}, \tag{40c}$$

$$f_{dy} = T_{S21}v_o + T_{S22}f_{oy}, \tag{40d}$$

where

$$T_{L11} = T_{L22} = \frac{\alpha(1 - r_\alpha) + a(2 - r_a) + (c^2/b)r_b}{\alpha r_\alpha + a r_a - (c^2/b)r_b}, \tag{41a}$$

$$T_{L12} = \frac{1}{\alpha r_\alpha + a r_a - (c^2/b)r_b}, \tag{41b}$$

$$T_{L21} = \frac{(\alpha(1 - 2r_\alpha) + a(2 - 2r_a))(\alpha + 2a - 2(c^2/b)r_b)}{\alpha r_\alpha + a r_a - (c^2/b)r_b}, \tag{41c}$$

$$T_{S11} = T_{S22} = \frac{\beta(1 - r_\beta) + b(2 - r_b) + (c^2/a)r_a}{\beta r_\beta + b r_b - (c^2/a)r_a}, \tag{42a}$$

$$T_{S12} = \frac{1}{\beta r_\beta + b r_b - (c^2/a)r_a}, \tag{42b}$$

$$T_{S21} = \frac{(\beta(1 - 2r_\beta) + b(2 - 2r_b))(\beta + 2b - 2(c^2/a)r_a)}{\beta r_\beta + b r_b - (c^2/a)r_a}. \tag{42c}$$

According to the longitudinal transfer matrix in Eq. (7), the longitudinal effective parameters can be defined as

$$m_L = -\frac{T_{L21}}{\omega^2},\tag{43a}$$

$$\alpha_{\text{eff}} = \frac{T_{L21}}{T_{L11} - 1}.\tag{43b}$$

Therefore, the longitudinal effective stiffness and mass can be derived as

$$m_L = \frac{(m_1 r_\alpha + m_2 r_a)\alpha_{\text{eff}}}{\alpha r_\alpha + a r_a - (c^2/b)r_b},$$

$$\alpha_{\text{eff}} = \alpha + 2a - 2(c^2/b)r_b.\tag{44a}$$

Additionally, according to the shear transfer matrix in Eq. (8), the shear effective parameters can be defined as

$$m_S = -\frac{T_{S21}}{\omega^2},\tag{45a}$$

$$\beta_{\text{eff}} = \frac{T_{S21}}{T_{S11} - 1}.\tag{45b}$$

Therefore, the shear effective stiffness and mass can be derived as

$$m_S = \frac{(m_1 r_\beta + m_2 r_b)\beta_{\text{eff}}}{\beta r_\beta + b r_b - (c^2/a)r_a},\tag{46a}$$

$$\beta_{\text{eff}} = \beta + 2b - 2(c^2/a)r_a.\tag{46b}$$

From the effective parameters shown in Eqs. (44) and (46), let us check whether the proposed unit can be used for the multimode incident case. In the previous section, it was shown that a metasurface unit whose effective parameters, m_L, α_{eff}, m_S, and β_{eff} can be freely adjusted from negative to positive values is required. From the equivalent stiffnesses α_{eff} and β_{eff} in Eqs. (44) and (46), it can be easily seen that those stiffnesses can be adjusted from negative to positive values owing to the resonance terms r_b and r_a. For instance, as frequency increases, $r_b = 2b/(2b - \omega^2 m_2)$ also changes so that α_{eff} is changed. At a frequency slightly lower than the resonance frequency of $\omega = \sqrt{2b/m_2}$, r_b and α_{eff} become positive and negative infinite values, respectively; subsequently, as frequency increases, the parameters suddenly change to opposite infinite values. Thus, by adjusting the values of b and m_2, the desired value of α_{eff}, either positive or negative, is achievable. In the same manner, β_{eff} can be freely adjusted from a negative to positive value by properly chosen a and m_2 values owing to the $r_a = 2a/(2a - \omega^2 m_2)$ term.

On the other hand, the equivalent masses m_L and m_S are defined in such complicated equations that it is hard to see how the equivalent mass can be tailored from positive to negative infinite values from Eqs. (44a) and (46a), as r_α, r_a,

r_β, and r_b are located in both numerator and denominator. However, one can notice that the resonance terms r_α, r_a, r_β, and r_b are multiplied by each other in the numerator (note that α_{eff} and β_{eff} contain r_b and r_a, respectively), while the resonance terms are simply summed in the denominator. Since the resonance terms are tunable from negative to positive infinite values, the higher order of resonance terms in the numerator indicates that the effective masses also can be tuned from negative to positive infinite values with the proper resonance terms, r_α, r_a, r_β, and r_b. Note that this analytic investigation suggests singularities around the frequencies where the denominators become zero, i.e., $\alpha r_\alpha + a r_a - (c^2/b)r_b$ or $\beta r_\beta + b r_b - (c^2/a)r_a$ become zero.

Before closing the theoretical investigations, the resonance mode corresponding to each effective parameter is studied to help the understanding of the proposed unit cell. To this end, the motion of each mass under longitudinal or shear wave incidence is focused upon. First, we assume the longitudinal elastic wave is incident at the left side of the unit. Since the unit has a symmetric configuration along the y axis, there is no mode coupling, i.e., only the longitudinal wave exists at the right side. Therefore, $v_o = v_d = 0$ holds for both sides and Eqs. (37b), (37d), and (37e) can be simplified as

$$v_1 = r_\beta(v_o + v_d) = 0,\tag{47a}$$

$$u_2 - u_3 = \frac{c}{a}r_a(v_o - v_d) = 0, \; u_2 = u_3,\tag{47b}$$

$$v_2 + v_3 = r_b(v_o + v_d) = 0, \; v_2 = -v_3.\tag{47c}$$

Substituting Eqs. (47a)–(47c) into Eqs. (37c) and (37f) yields

$$u_2 = u_3 = r_a(u_o + u_d)/2,\tag{48a}$$

$$v_2 = -v_3 = (c/b)r_b(u_o - u_d)/2.\tag{48b}$$

The corresponding motion is plotted in Fig. 2(b). According to Eq. (48), the outer resonators move symmetrically as can be seen in Fig. 2(b). The vertical movements of the outer resonators will push (or pull) the left and right boundaries, and subsequently the effective mass and stiffness are modified according to the vertical resonance state. In addition, the horizontal movements of both inner and outer resonators, Eqs. (47a) and (48a), show the symmetric horizontal deformation that affects overall inertia and the effective mass according to their resonance motions.

On the other hand, for the shear wave incident case, $u_o = u_d = 0$ holds. Accordingly, Eqs. (37a), (37c), and

(37f) can be simplified as

$$u_1 = \frac{\alpha}{2\alpha - \omega^2 m_1}(u_o + u_d) = 0, \tag{49a}$$

$$u_2 + u_3 = \frac{2a}{2a - \omega^2 m_2}(u_o + u_d) = 0, \; u_2 = -u_3, \tag{49b}$$

$$v_2 - v_3 = \frac{2c}{2b - \omega^2 m_2}(u_o - u_d) = 0, \; v_2 = v_3. \tag{49c}$$

Again, substituting Eqs. (49a)–(49c) into Eqs. (37d) and (37e) yields

$$u_2 = -u_3 = (c/a)r_a(v_o - v_d)/2, \tag{50a}$$

$$v_2 = v_3 = r_b(v_o + v_d)/2. \tag{50b}$$

Here, the shear effective stiffness is tuned by the horizontal resonance state, r_a in Eq. (46b), which implies that the opposite horizontal movement of the outer resonator tunes the shear effective stiffness. Figure 2(c) briefly describes how the opposite horizontal movement affects the shear effective stiffness. By observing the compressions and tensions of the diagonal springs, one can find that the x-directional force at each boundary is canceled and only the y-directional forces remain. Accordingly, the shear effective stiffness is tuned by horizontal resonance of the outer resonators with this procedure. Furthermore, the vertical resonances of both inner and outer resonators affect the shear effective stiffness owing to the change of the y-directional inertia. Additional numerical validations for the Eqs. (44) and (46) are provided in the Supplemental Material [33].

III. MODE-SELECTIVE METASURFACE

In the previous section, we showed that the unit shown in Fig. 2(a) can be tailored to have any desired effective parameters so that elastic metasurface under the multimode incidence case is feasible. In this section, mode-selective metasurfaces are designed with the unit in Fig. 2(a). As explained earlier, a mode-selective metasurface is an elastic metasurface that can tailor the desired wave mode but filter out the other undesired mode. Here, two mode-selective metasurfaces are designed. The first one is the longitudinal-mode-selective metasurface (referred to as LMS), which tailors longitudinal waves but filters out shear waves. The other one is the shear-mode-selective metasurface (referred to as SMS), which tailors shear waves, filtering out longitudinal waves.

One may think other metasurfaces, such as an elastic metasurface tailoring both wave modes simultaneously, would be much more important. However, the practical importance of such elastic metasurfaces is much lower than expected. The main reason is the mode coupling: although the metasurface successfully tailors both modes along the desired directions, both longitudinal and shear waves are transmitted for each incident mode owing to mode coupling. Thus, there is almost no difference between the transmitted waves for longitudinal or shear wave incidence, i.e., simultaneous tailoring of both wave modes is not important. Furthermore, in almost all applications, there is no elastic transducer that can generate only a single wave mode. This is extremely critical in various applications where various reflections take place such that different wave modes are extremely hard to distinguish. Therefore, a certain wave mode is focused while another wave mode is considered as noise, and filtering out the other wave mode is usually preferable to tailoring it. These are the reasons we focus on the mode-selective metasurface while simultaneous tailoring of both wave modes is also possible.

A. Longitudinal-mode-selective metasurface

First, a LMS is designed. To this end, the metasurface units should be designed to provide full transmission and the desired phase shift for longitudinal wave incidence but zero transmission for shear mode incidence. Accordingly, we extend the mass-spring unit shown in Fig. 2(a) as a continuum metasurface unit made of aluminum, as shown in Fig. 3. The overall configuration seems to be similar to those in previous studies [24,30], but unlike the previous ones, the zero-transmission condition for shear wave incidence is additionally considered so that the detailed geometries are different.

To design the detailed geometry of the metasurface unit, perhaps the analytic equations shown in the previous section can be used. However, in the actual design, a very precise design approach is required since the resonance motions are highly sensitive even with very small geometric changes. Unfortunately, the analytic equations are not precise enough because the actual continuum unit cannot be clearly distinguished into masses or springs. If the parts of the unit are clearly distinguishable, the analytic equations in Eqs. (44) and (46) could be used to design the metasurface since any change in the spring part will not alter the mass parameters m_1, m_2, and any change in the mass part will not alter the spring coefficients, such as a, b, and c. However, the parts of the unit are not clearly distinguishable and any change to design parameters causes changes to all coefficients, which makes it impossible to design the metasurface units with the analytic equations. Thus, the metasurface units are designed by a numerical method of size optimization. Here, we adopt the well-known size optimization algorithm, particle swarm optimization (PSO). For more details about PSO, see the Supplemental Material [33].

The detailed design procedures are as follows. First, with the current design, one-dimensional time-harmonic wave simulation is carried out. The wave simulation settings are shown in Fig. 4(a). At the upper and lower boundaries, the periodic continuum condition is applied
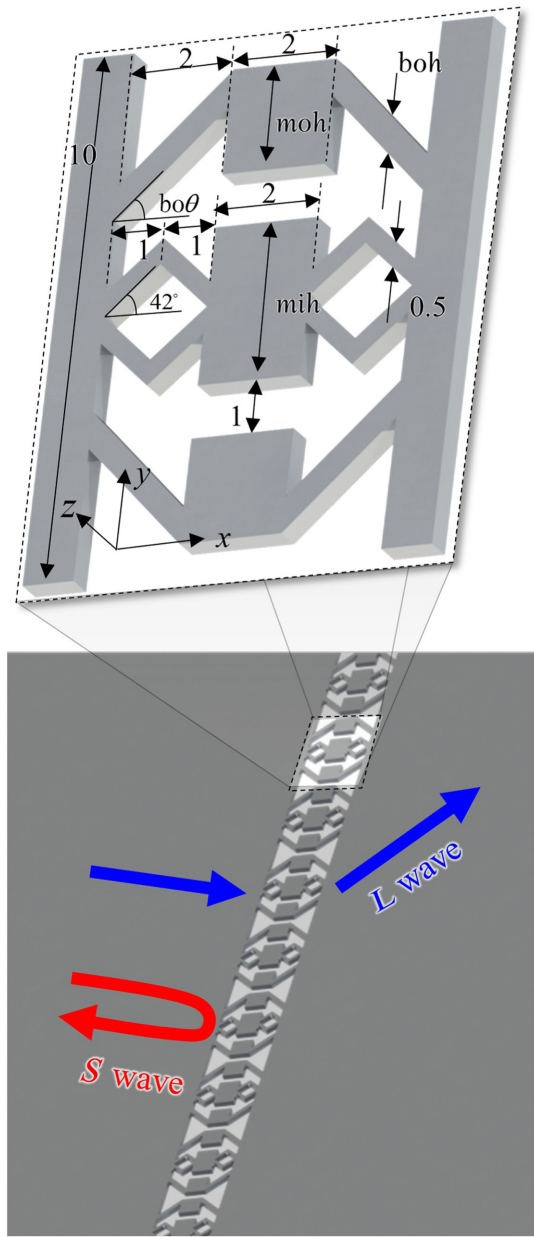
FIG. 3. The unit-cell structure of the LMS. Sizes are given in millimeters and the z axis thickness is 1 mm.
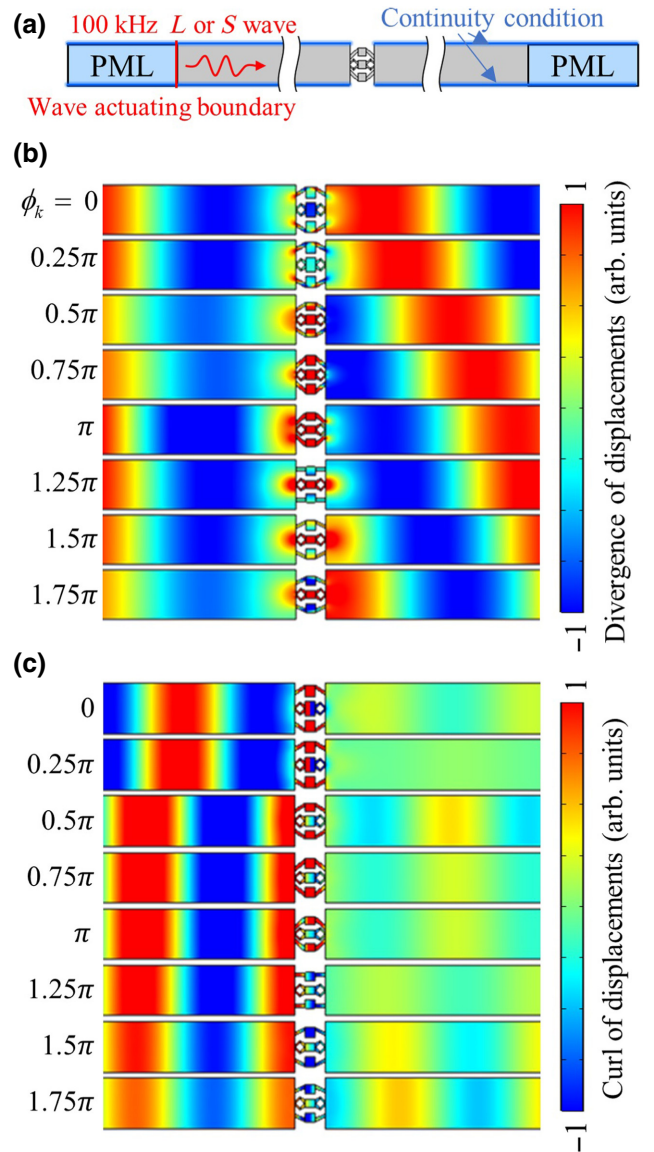

FIG. 4. (a) The one-dimensional numerical simulation settings for each longitudinal metasurface unit. The simulation results for (b) longitudinal and (c) shear incidence cases.

to consider where the unit is infinitely arranged along the y direction so that perfect plane-wave simulation is possible. In addition, at the left and right ends, a perfectly matched layer (PML) is placed to eliminate any undesired reflections. With these settings, two simulations are carried out, one for longitudinal wave excitation and the other for shear wave excitation, at a frequency of 100 kHz. From the longitudinal wave simulation, the amount of the longitudinal wave reflection and the transmitted longitudinal wave's phase shift are measured with the well-known two-points method [34]. Also, the amount of the shear wave transmission is measured from the shear wave simulation.

After the simulations, the design parameters can be selected by the PSO algorithm. Here, the multiobjective optimization should be carried out to satisfy three requirements: full transmission and the desired phase shift for the longitudinal wave and zero transmission for the shear wave. Thus, we define the following objective function that should be minimized during the PSO process as

$$f_L(\mathbf{X}) = R_L(\mathbf{X}) + |\phi_L(\mathbf{X}) - \phi_k| + T_S(\mathbf{X}), \qquad (51)$$

where R_L refers to the reflection of the longitudinal wave, ϕ_L and ϕ_k refer to the phase shift of the current unit and the desired value, and T_S refers to the transmission of the shear

TABLE I.   The realized values and design parameters of each LMS unit cell.

Ideal value	Realized values			Design variables			
ϕ_L (π rad)	$\lvert T_L \rvert$	ϕ_L (π rad)	$\lvert R_S \rvert$	mih (mm)	moh (mm)	boh (mm)	boθ (deg)
0	0.994	0.033	0.978	2.78	2.30	0.64	34.56
0.25	1.000	0.207	0.998	2.78	2.30	0.81	29.75
0.5	0.922	0.595	0.900	1.94	1.61	0.64	32.65
0.75	0.955	0.812	0.970	1.87	2.00	0.90	41.09
1	0.906	1.077	0.976	1.60	1.77	0.92	42.00
1.25	0.998	1.194	0.987	1.77	1.71	0.68	6.30
1.5	0.989	1.434	0.929	1.71	2.08	0.60	27.20
1.75	0.937	1.662	0.862	1.60	1.88	0.66	25.67

wave. R_L, ϕ_L, and T_S are numerically measured from the simulation, and ϕ_k is predefined to form the desired phase gradient. With the objective function, PSO updates four design variables, mih, moh, boh, and boθ shown in Fig. 3 to minimize $f_L(\mathbf{X})$. After the design variables are updated, the whole process is repeated till convergence. Note that the geometric parameters are achieved for the given frequency, so if the frequency changes, one may redesign the metasurface unit. However, the overall configuration is still valid since the theory and the resonator systems are not dependent on the frequency. Also, one may simply scale the metasurface unit according to the wavelength without redesign. This scaling is valid for low frequencies where the wavelength is much larger than the thickness of the plate so that a higher elastic wave mode is not involved at all.

With the design process, the LMS is designed. First, units are designed with phase shifts of $\phi_k =$ 0, 0.25π, 0.5π, 0.75π, π, 1.25π, 1.5π, and 1.75π. Table I summarizes the final design parameters of each unit, and Fig. 4 plots the corresponding one-dimensional wave simulation results. As can be seen in Fig. 4(b), all units have almost full transmission with the desired phase shifts for longitudinal wave incidence. In addition, for the shear wave incidence cases, all units exhibit very low transmission as desired. Data in Table I show that all units show a transmission ratio of more than 0.9 for longitudinal waves. Also, the reflection ratio is shown to be around or larger than 0.9, with the minimum value of 0.862. These values show that sufficiently large transmission and reflection are achieved to realize the desired mode-selective metasurface.

From the successful designs of each unit, the LMS is proposed by arranging the whole unit. Figure 5(a) shows the wave simulation settings to check the performance of the proposed LMS. Here, the metasurface is placed in the middle of a 2×1 m^2 aluminum plate, surrounded by a PML to avoid any undesired reflections. At the left side of the metasurface, a 10-cm-long wave source is placed at 0.5 m from the metasurface. Two simulations are carried

out, one for longitudinal wave excitation and the other for shear wave excitation at the wave source. In all simulations, time-harmonic simulation is conducted with COMSOL Multiphysics.

The simulation result for the longitudinal incident case is shown in Fig. 5(b). Here, the divergence of displacement field is plotted to show the longitudinal wave mode only. Clearly, the longitudinal wave is fully tailored at the LMS. The numerically calculated refraction angle is 42°, which agrees well with the analytically predicted refraction angle of 42.4° according to the generalized Snell's law [1]. In addition, the simulation with the shear incidence case in Fig. 5(c) shows that the shear wave is almost filtered out with negligible transmission. It should be emphasized that in Fig. 5(c), there are almost no scattered shear waves propagating along various directions. This strongly indicates that the proposed metasurface is well designed for both wave modes; otherwise, the transmitted waves would be scattered along various directions. From these observations, it can be concluded that the proposed LMS is well designed.

To further check the amount of the reflected waves, the same simulations are repeated for the obliquely incident case. Since our metasurface is designed based on the normal incidence case, its performance becomes worse as the incident angle is increased. To understand this point, let us recall that the background physics of our metasurface is based on the transfer matrix, which is defined by the displacements and forces at each boundary. For small incident angles, the displacements and forces at the boundary are not largely altered from the normally incident case so that the metasurface still shows good performance. As can be seen in Fig. 6(a), the longitudinal and shear waves are generated with a $-10°$ incident angle. Again, the longitudinal wave is tailored along the theoretically predicted angle, 30.0°. In addition, although the performance of blocking the shear wave is lowered, since the units are designed for normally incident waves, most of the shear wave is still filtered out, i.e., we confirm the LMS covers slight angle changes.
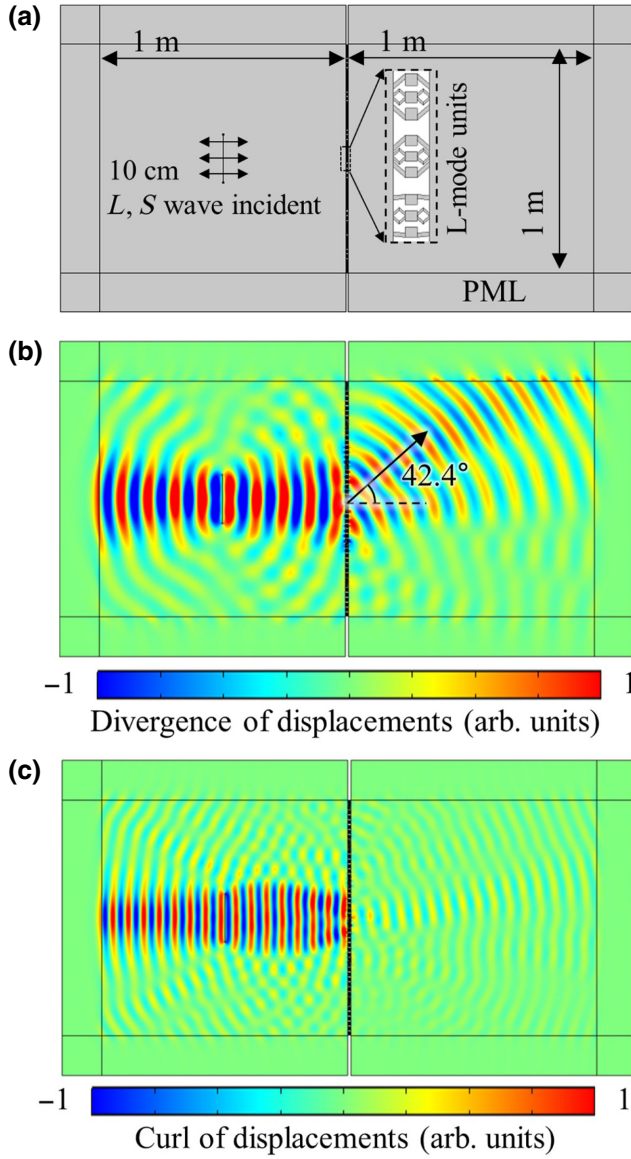
FIG. 5. (a) Two-dimensional wave field simulation settings of the LMS. The simulation results for the (b) longitudinal and (c) shear incidence cases.

FIG. 6. (a) The simulation settings and (b),(c) results of the oblique incidence case for the LMS metasurface.

B. Shear-mode-selective metasurface

Finally, a SMS that can tailor incident shear waves while filtering out incident longitudinal waves is designed. The metasurface unit is slightly changed, as shown in Fig. 7, so that the vertical resonance motion (which dominates the shear effective mass) is facilitated more than the unit in Fig. 3. With the unit, the detailed geometry is designed to provide full transmission and the desired phase shift for shear wave incidence and zero transmission for longitudinal wave incidence.

The design procedure is the same as for the LMS. The one-dimensional wave simulation setting shown in
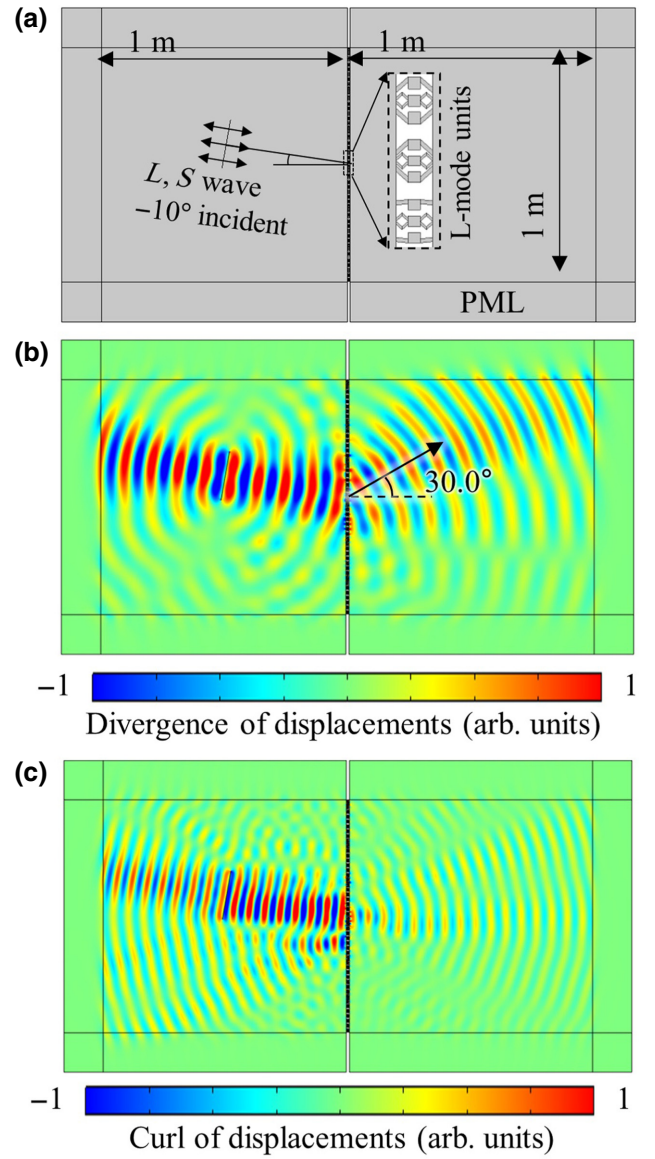
Fig. 8(a) is modeled, and two simulations with longitudinal and shear wave excitation are conducted at a frequency of 100 kHz. From the shear wave excitation, the shear wave's reflection and phase shift are measured. Also, from the longitudinal wave excitation, the longitudinal wave's transmission is measured. After the simulation, PSO is carried out with the objective function defined as

$$f_S(\mathbf{X}) = R_S(\mathbf{X}) + |\phi_S(\mathbf{X}) - \phi_k| + T_L(\mathbf{X}), \qquad (52)$$

where R_S and ϕ_S are the reflection and phase shift of the shear wave, whereas T_L refers to the transmission of the longitudinal wave. For improved design, a design variable of bih is now additionally considered with the design variables of mih, moh, boh, and boθ, as shown in Fig. 7.
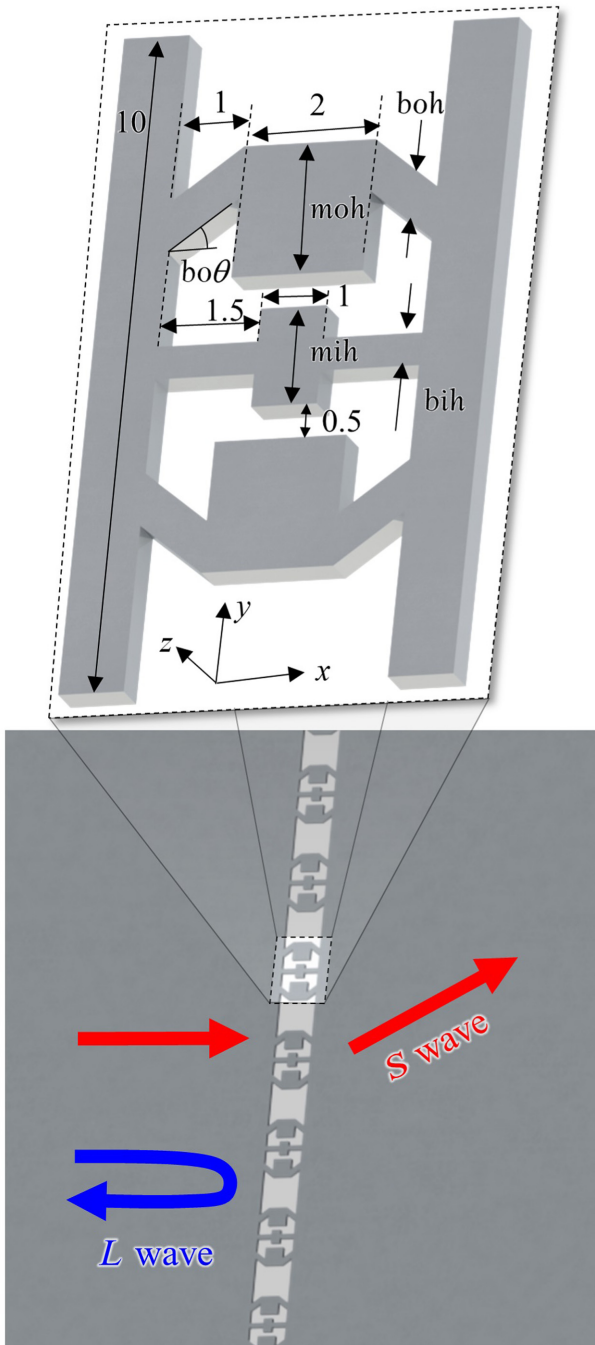
FIG. 7.   The unit-cell structure of the SMS. Sizes are given in millimeters and the *z* axis thickness is 1 mm.
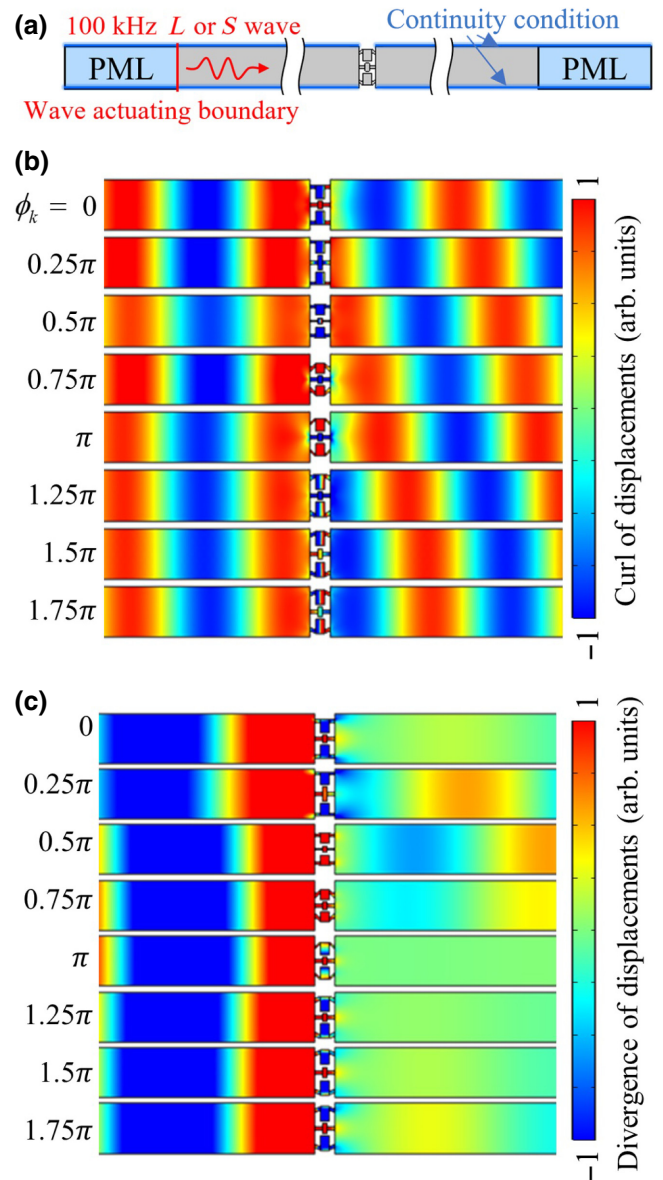

FIG. 8.   (a) The one-dimensional numerical simulation settings for each shear metasurface unit. The simulation results for the (b) shear and (c) longitudinal incidence cases.

Table II summarizes the desired units for the same phase shifts as in Table I. From the one-dimensional wave simulation results in Figs. 8(b) and 8(c), it seems that all units exhibit sufficiently high transmission, desired phase shifts for shear incidence, and sufficiently low transmission for the longitudinal wave incidence. For all units, the shear waves are shown to have transmission higher than 0.9, while the longitudinal waves are shown to have reflection higher than 0.84. As a result, it can be concluded that all units are properly designed.

By arranging the designed units, the SMS is proposed. Figure 9(a) is the simulation setting to check the performance of the proposed SMS. The simulation setting is same as the previous one in Fig. 5(a); the only difference is that the metasurface is changed to the SMS. Figures 9(b) and 9(c) show the simulation results for the longitudinal and shear wave incidence, respectively. Clearly, the incident shear wave is tailored while the incident longitudinal wave is filtered out. The refraction angle of the shear wave is numerically measured as 23°, which follows well the analytically predicted angle of 23.0°. Also, there

TABLE II. The realized values and design parameters of each SMS unit cell.

Ideal value	Realized values			Design variables				
ϕ_S (π rad)	$|T_S|$	ϕ_S (π rad)	$|R_L|$	mih (mm)	bih (mm)	moh (mm)	boh (mm)	boθ (deg)
0	0.979	−0.020	0.990	1.52	0.5	2.70	0.60	6.66
0.25	0.975	0.218	0.978	2.90	0.5	2.50	0.53	1.00
0.5	0.961	0.555	0.847	1.31	0.2	2.02	0.50	9.44
0.75	0.913	0.835	0.946	1.63	0.5	1.88	0.77	42.83
1	0.998	1.001	1.000	1.60	0.5	2.49	0.50	45.00
1.25	0.999	1.338	0.999	1.57	0.5	2.90	0.71	25.76
1.5	0.997	1.575	0.993	2.14	0.5	2.90	0.71	22.50
1.75	0.954	1.645	0.966	1.98	0.5	2.80	0.71	27.69

are almost no scattered waves for the incident longitudinal wave, validating our SMS.

Figure 10 plots the simulation results for the obliquely incident wave. As shown in Fig. 10(a), the longitudinal and shear waves are generated into the SMS with a −10° incident angle. Figures 10(b) and 10(c) show the results for the longitudinal and shear incidence cases, respectively. Obviously, the incident longitudinal wave is perfectly blocked whereas the shear wave is clearly tailored along the theoretically predicted angle, 12.5°, which implies that the SMS works perfectly with slight angle changes.

IV. EXPERIMENTAL VALIDATIONS

Finally, we conduct experiments on the mode-selective metasurfaces. Figure 11(a) shows a schematic diagram and actual photos of the experimental setups. As shown in Fig. 11(a), each mode-selective metasurface is fabricated in the middle of two identical 2×1 m^2 aluminum plates with 1-mm thickness, i.e., two aluminum plates, one for LMS and the other for SMS, are separately fabricated. Here, it should be noted that the metasurface designs given in Tables I and II require too high fabrication resolution, which is almost impossible with the available fabrication process. Thus, the frequency is lowered from 100 to 50 kHz so that the overall metasurface size is doubled. As a result, the metasurfaces are successfully fabricated by laser beam machining (Bysprint Fiber 3015, Bystronic).

Based on the fabricated metasurface, the following four cases are considered during the experiments:

(1) Longitudinal wave incidence on the LMS, and measurement of transmitted longitudinal wave
(2) Shear wave incidence on the LMS, and measurement of transmitted shear wave
(3) Longitudinal wave incidence on the SMS, and measurement of transmitted longitudinal wave
(4) Shear wave incidence on the SMS, and measurement of transmitted shear wave

For all cases, the wave actuation is made by an elastic wave transducer located 0.5 m from the center of the metasurface. Also, the measurements are carried out every 10° and at 0.3 m from the center of the fabricated metasurface, as shown by the white dots in Fig. 11(a). For the wave transducer, the magnetostrictive patch transducer (MPT) and the electromagnetic acoustic transducer (EMAT) are adopted as the wave actuation and measurement devices, respectively. The MPT can imitate an ideal line source in the experiments since it can mainly generate the selected wave mode only along the desired direction [35]. Also, the EMAT sensor can selectively measure the desired wave mode using a noncontact mechanism while filtering out the unwanted wave modes [36].

The experimental procedure is as follows. First, the four-cycle sinusoidal burst signal is generated by the laptop and amplified by the pulser-receiver system (EMS-PR2000). The amplified signal is sent to the self-made MPT to actuate the desired longitudinal or shear wave. After the elastic wave propagates through the LMS or SMS, the EMAT sensor (which is set to measure the corresponding wave mode) measures the transmitted wave. The measured signal is amplified again with the same pulser-receiver system and plotted on the oscilloscope (HDO4034A, Teledyne LeCroy). After that, the measured signals are postprocessed by fast Fourier transform to estimate the 50-kHz component only. Finally, the measured values are normalized with the maximum value of the measured data. To be specific, the whole longitudinal amplitudes in both LMS and SMS results are normalized by the maximum value at 40° in the left figure of Fig. 11(b), while the shear amplitudes are normalized by the maximum value at 20° in the right figure of Fig. 11(b).

Figure 11(b) plots the experimental results. In the LMS (plotted on the left), it can be clearly seen that the transmitted longitudinal wave is much larger than the transmitted shear wave. A very small amount of the shear wave is measured for all angles, validating that the metasurface successfully filters out the undesired shear wave. On the other hand, the measured longitudinal wave has maximum value along a certain angle, which is exactly same as the
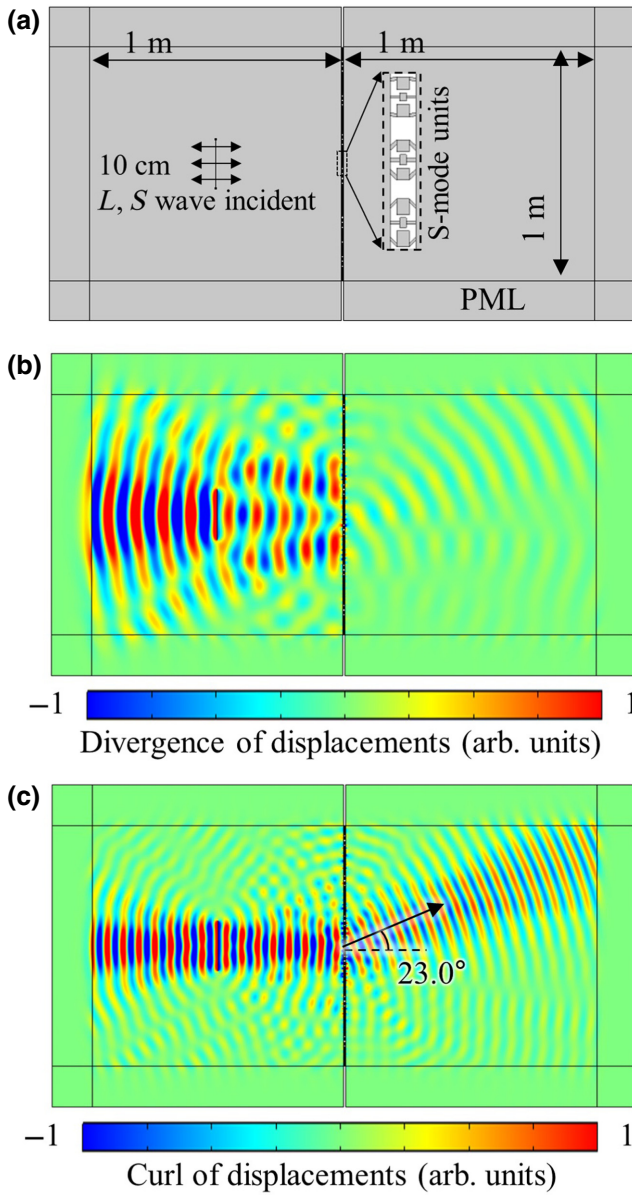
FIG. 9.   (a) Two-dimensional wave field simulation settings of the SMS. The simulation results for the (b) longitudinal and (c) shear incidence cases.

FIG. 10.   (a) The simulation settings and (b),(c) results of the oblique incidence case for the SMS.

angle predicted by the generalized Snell's law (depicted as the vertical black line). Similar results can be found for the SMS (plotted on the right). The longitudinal wave is clearly smaller than the shear wave, and the shear wave is well confined along a certain angle. Again, this angle is same as the angle predicted by the generalized Snell's law. The results in Fig. 11(b) clearly illustrate that the proposed mode-selective metasurfaces manipulate the desired wave modes well while filtering out the undesired wave modes.

Although the experimental results clearly validate the proposed mode-selective metasurfaces, experimental results do not show the detailed wave propagation. To this
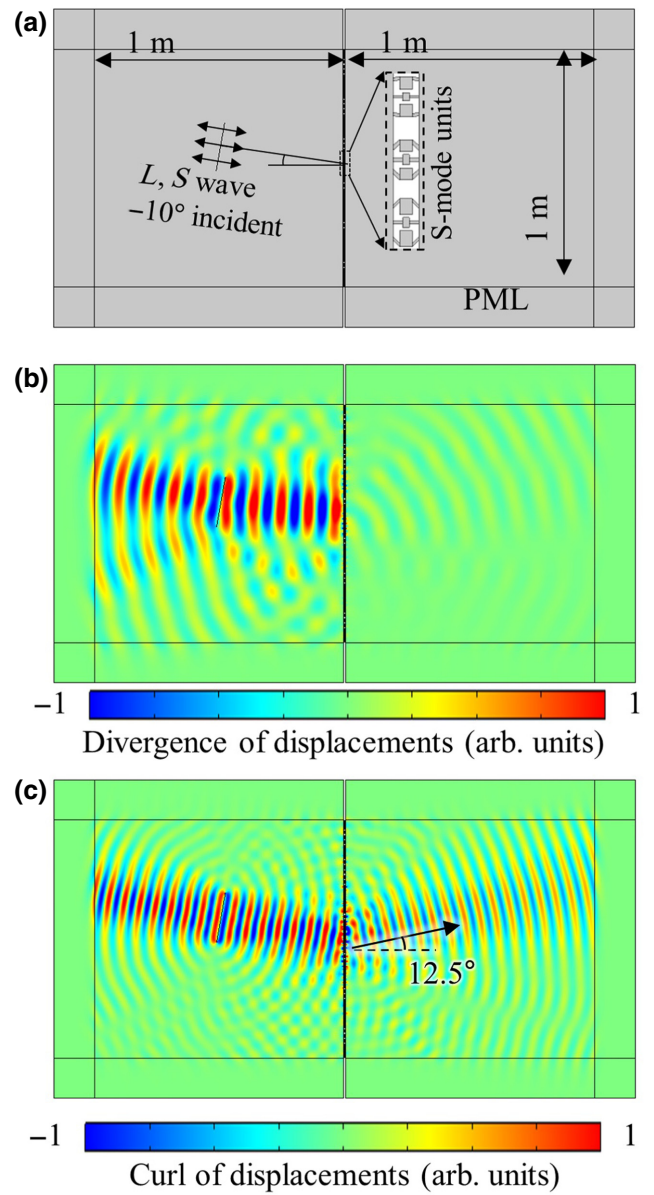
end, the time-transient simulations by another commercial program, ABAQUS, are also carried out. See the Supplemental Material [33] for detailed visualizations of wave propagation through the mode-selective metasurfaces.

V. CONCLUSION

In this work, we suggest mode-selective metasurfaces for longitudinal and shear waves. First, from the theoretical study for each wave, we find the metasurface unit whose effective stiffness and mass can be tuned from negative to positive infinite values are needed. Therefore, the ideal resonator system composed of the outer resonator
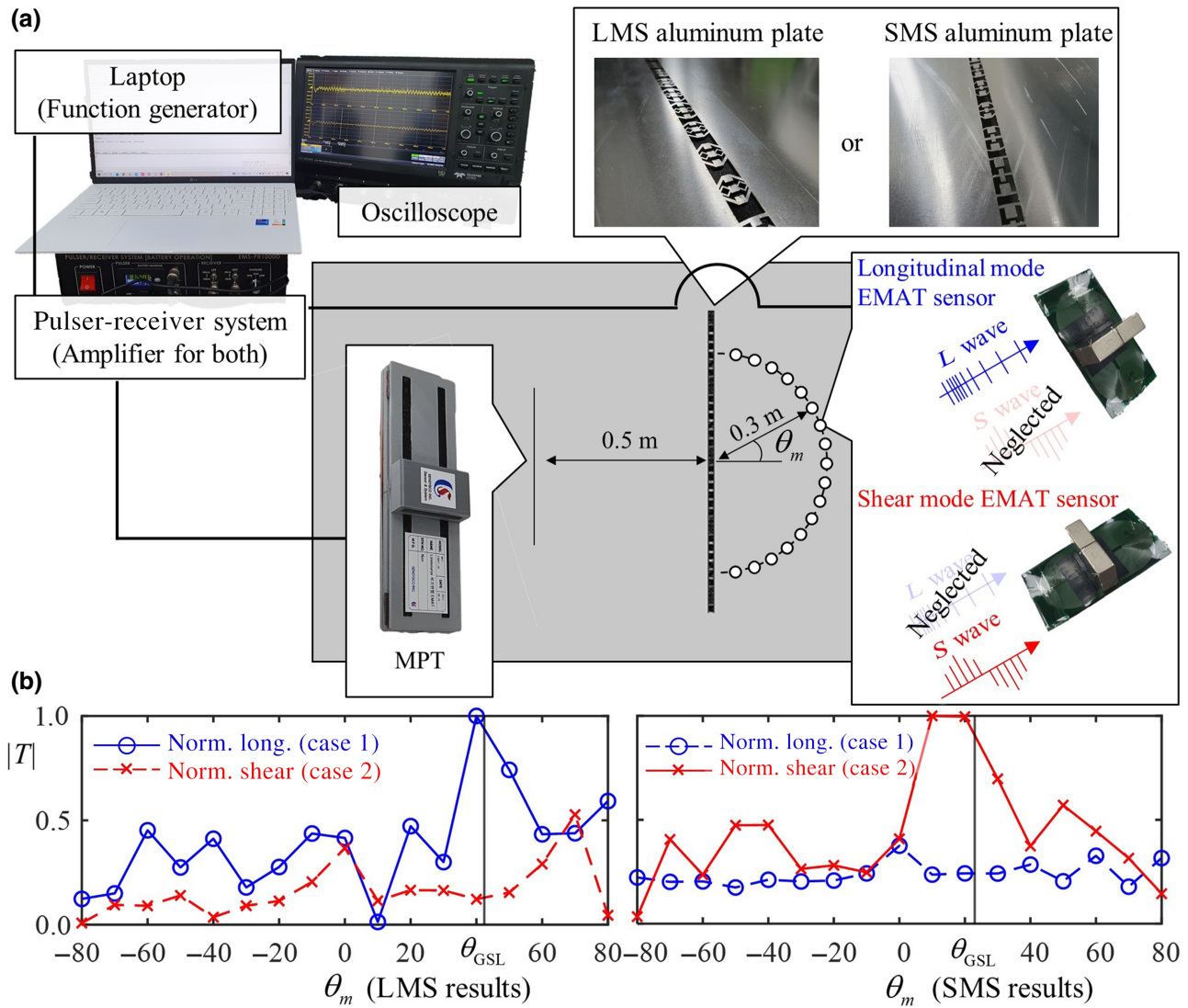
(a)

(b)

FIG. 11. (a) The detailed figure of the experimental setups, (b) plot of the experimentally measured longitudinal and shear waves. θ_{GSL} refers to the theoretically predicted angle by the generalized Snell's law.

and inner resonator are suggested. By utilizing vertical resonance of the outer resonator and horizontal resonance of the inner resonator, the longitudinal effective parameters can be tuned, while the rotational (horizontal) resonance of the outer resonator and vertical resonance of the inner resonator tunes the shear effective parameters. Based on the ideal modeling, the continuum structures for both mode-selective metasurfaces are designed. Using the PSO algorithm, design parameters that achieve the proper phase shift and full transmission for the target wave and full reflection for the unwanted wave can be found. Subsequently, both mode-selective metasurfaces designed by arranging the unit cells are numerically validated. Both mode-selective metasurfaces tailor each desired wave well according to the generalized Snell's law, while filtering out the unwanted waves. In addition, we numerically confirm

both metasurfaces still function well with slight incident angle differences. Finally, both mode-selective metasurfaces (LMS and SMS) are fabricated and experimentally validated.

We expect that our metasurface can provide practical advances in various applications. To be specific, since there is no elastic transducer that can generate only a single mode, mode filtering techniques have been demanded in elastic wave applications. Here, the simultaneous mode filtering will improve the wave tailoring performance of elastic metasurfaces.

[1] N. Yu, P. Genevet, M. Kats, F. Aieta, J. Tetienne, F. Capasso, and Z. Gaburro, Light propagation with phase discontinuities: Generalized laws of reflection and refraction, Science **334**, 333 (2011).

[2] J. Hu, S. Bandyopadhyay, Y. -h. Liu, and Shao, A review on metasurface: From principle to smart metadevices, Front. Phys. **8**, 586087 (2021).

[3] C. L. Holloway, E. F. Kuester, J. A. Gordon, J. O'Hara, J. Booth, and D. R. Smith, An overview of the theory and applications of metasurfaces: The two-dimensional equivalents of metamaterials, IEEE Antennas Propag. Mag. **54**, 10 (2012).

[4] F. Ding, A. Pors, and S. I. Bozhevolnyi, Gradient metasurfaces: A review of fundamentals and applications, Rep. Prog. Phys. **81**, 026401 (2018).

[5] S. Sun, K.-Y. Yang, C.-M. Wang, T.-K. Juan, W. T. Chen, C. Y. Liao, Q. He, S. Xiao, W.-T. Kung, G.-Y. Guo, et al., High-efficiency broadband anomalous reflection by gradient meta-surfaces, Nano Lett. **12**, 6223 (2012).

[6] L. B. Yan, W. M. Zhu, P. C. Wu, H. Cai, Y. D. Gu, L. K. Chin, Z. X. Shen, P. H. J. Chong, Z. C. Yang, W. Ser, et al., Adaptable metasurface for dynamic anomalous reflection, Appl. Phys. Lett. **110**, 201904 (2017).

[7] D. Sell, J. Yang, E. W. Wang, T. Phan, S. Doshay, and J. A. Fan, Ultra-high-efficiency anomalous refraction with dielectric metasurfaces, ACS Photonics **5**, 2402 (2018).

[8] H. F. Zhu and F. Semperlotti, Anomalous Refraction of Acoustic Guided Waves in Solids with Geometrically Tapered Metasurfaces, Phys. Rev. Lett. **117**, 034302 (2016).

[9] V. S. Asadchy, M. Albooyeh, S. N. Tcvetkova, A. DiazRubio, Y. Radi, and S. A. Tretyakov, Perfect control of reflection and refraction using spatially dispersive metasurfaces, Phys. Rev. B **94**, 075142 (2016).

[10] J. P. S. Wong, A. Epstein, and G. V. Eleftheriades, Reflectionless wide-angle refracting metasurfaces, IEEE Antennas Wireless Propag. Lett. **15**, 1293 (2016).

[11] E. Bok, J. J. Park, H. Choi, C. K. Han, O. B. Wright, and S. H. Lee, Metasurface for Water-to-Air Sound Transmission, Phys. Rev. Lett **120**, 044302 (2018).

[12] A. H. Dorrah, M. Chen, and G. V. Eleftheriades, Bianisotropic Huygens' metasurface for wideband impedance matching between two dielectric media, IEEE Trans. Antennas Propag. **66**, 4729 (2018).

[13] M. Ebrahimpouri, L. F. Herran, and O. Quevedo-Teruel, Wide-angle impedance matching using glide-symmetric metasurfaces, IEEE Microwave Wirel. Comp. Lett. **30**, 8 (2020).

[14] S. W. Lee, Y. J. Shin, H. W. Park, H. M. Seung, and J. H. Oh, Full-wave Tailoring Between Different Elastic Media: A Double-Unit Elastic Metasurface, Phys. Rev. Appl. **16**, 064013 (2021).

[15] W. Wan, J. Gao, and X. Yang, Metasurface holograms for holographic imaging, Adv. Opt. Mater. **5**, 1700541 (2017).

[16] L. Huang, S. Zhang, and T. Zentgraf, Metasurface holography: From fundamentals to applications, Nanophotonics **7**, 1169 (2018).

[17] G.-Y. Lee, J. Sung, and B. Lee, Recent advances in metasurface hologram technologies (Invited paper), ETRI J. **41**, 10 (2019).

[18] S. W. Fan, Y. F. Zhu, L. Y. Cao, Y. F. Wang, A. L. Chen, A. Merkel, Y. S. Wang, and B. Assouar, Broadband tunable lossy metasurface with independent amplitude and phase modulations for acoustic holography, Smart. Mater. Struct **29**, 105038 (2020).

[19] P. Y. Chen, J. Soric, Y. R. Padooru, H. M. Bernety, A. B. Yakovlev, and A. Alù, Nanostructured graphene metasurface for tunable terahertz cloaking, New J. Phys. **15**, 123029 (2013).

[20] Y. Yang, H. Wang, F. Yu, Z. Xu, and H. Chen, A metasurface carpet cloak for electromagnetic, acoustic and water waves, Sci. Rep. **6**, 20219 (2016).

[21] H. Esfahlani, S. Karkar, H. Lissek, and J. R. Mosig, Acoustic carpet cloak based on an ultrathin metasurface, Phys. Rev. B **94**, 014302 (2016).

[22] S. W. Fan, S. D. Zhao, L. Cao, Y. Zhu, A. L. Chen, Y. F. Wang, K. Donda, Y. S. Wang, and B. Assouar, Reconfigurable curved metasurface for acoustic cloaking and illusion, Phys. Rev. B **101**, 024104 (2020).

[23] H. Lee, J. K. Lee, H. M. Seung, and Y. Y. Kim, Mass-stiffness substructuring of an elastic metasurface for full transmission beam steering, J. Mech. Phys. Solids **112**, 577 (2018).

[24] S. W. Lee and J. H. Oh, Single-layer elastic metasurface with double negativity for anomalous refraction, J. Phys. D: Appl. Phys. **53**, 265301 (2020).

[25] X. Su, Z. Lu, and A. N. Norris, Elastic metasurfaces for splitting SV- and P-waves in elastic solids, J. Appl. Phys. **123**, 091701 (2018).

[26] J. Zhang, X. Su, Y. L. Liu, Y. X. Zhao, X. Jing, and N. Hu, Metasurface constituted by thin composite beams to steer flexural waves in thin plates, Int. J. Solids Struct **162**, 14 (2018).

[27] L. Cao, Z. Yang, Y. Xu, and B. Assouar, Deflecting flexural wave with high transmission by using pillared elastic metasurface, Smart Mater. Struct. **27**, 075051 (2018).

[28] L. Cao, Z. Yang, Y. Xu, Z. Chen, Y. Zhu, S.-W. Fan, K. Donda, B. Vincent, and B. Assouar, Pillared elastic metasurface with constructive interference for flexural wave manipulation, Mech. Syst. Signal Proc. **146**, 107035 (2021).

[29] M. S. Kim, W. R. Lee, Y. Y. Kim, and J. H. Oh, Transmodal elastic metasurface for broad angle total mode conversion, Appl. Phys. Lett **112**, 241905 (2018).

[30] S. W. Lee, H. M. Seung, W. Choi, M. Kim, and J. H. Oh, Broad-angle refractive transmodal elastic metasurface, Appl. Phys. Lett **117**, 213502 (2020).

[31] L. Cao, Y. Zhu, Y. Xu, S. W. Fan, Z. Yang, and B. Assouar, Elastic bound state in the continuum with perfect mode conversion, J. Mech. Phys. Solids **154,** 104502 (2021).

[32] J. Rong and W. Ye, Multifunctional elastic metasurface design with topology optimization, Acta. Mater. **185,** 382 (2020).

[33] See Supplemental Material at http://link.aps.org/supplemental/10.1103/PhysRevApplied.19.014024 for the detailed procedure of the PSO algorithm, numerical validations on the mass-spring system, and time-transient simulations for visualizing wave propagations.

[34] B. Lundberg and A. Henchoz, Analysis of elastic waves from two-point strain measurement, Exp. Mech **17,** 213 (1977).

[35] Y. Y. Kim and Y. E. Kwon, Review of magnetostrictive patch transducers and applications in ultrasonic nondestructive testing of waveguides, Ultrasonics **62,** 3 (2015).

[36] M. Hirao and H. Ogi, *EMATS for science and industry* (Kluwer Academic Publishers, Boston, 2003).